ARCHIVIO ISTITUZIONALE
DELLA RICERCA

Alma Mater Studiorum Università di Bologna
Archivio istituzionale della ricerca

Probing the Metal/Oxide Interface of IrCoCeOx in N2H4·H2O Decomposition: An Experimental and Computational Study

This is the final peer-reviewed author's accepted manuscript (postprint) of the following publication:

Published Version:
Bellomi, S., Cano-Blanco, D.C., Barlocco, I., Delgado, J.J., Chen, X., Prati, L., et al. (2024). Probing the Metal/Oxide Interface of IrCoCeOx in N2H4·H2O Decomposition: An Experimental and Computational Study. ACS APPLIED MATERIALS & INTERFACES, 16, 54897-54906 [10.1021/acsami.4c12306].

Availability:
This version is available at: https://hdl.handle.net/11585/1037013 since: 2026-02-10

Published:
DOI: http://doi.org/10.1021/acsami.4c12306

Terms of use:

Some rights reserved. The terms and conditions for the reuse of this version of the manuscript are specified in the publishing policy. For all terms of use and more information see the publisher's website.

This item was downloaded from IRIS Università di Bologna (https://cris.unibo.it/).
When citing, please refer to the published version.

(Article begins on next page)

29 April 2026

Probing the metal/oxide interface of $IrCoCeO_x$ in the $N_2H_4 \cdot H_2O$ decomposition: an experimental and computational study

Silvio Bellomi[a], Daniel C. Cano-Blanco[b,c] , Ilaria Barlocco[a], Juan J. Delgado[d], Xiaowei Chen[d], Laura Prati[a], Davide Ferri[b], Nikolaos Dimitratos[e,f], Alberto Roldan[g], Alberto Villa[a]**

[a] Dipartimento di Chimica, Università degli Studi di Milano, via Golgi 19, I-20133, Milano, Italy

[b] Paul Scherrer Institut, PSI Center for Energy and Environmental Sciences, CH-5232, Villigen PSI, Switzerland

[c] École polytechnique fédérale de Lausanne (EPFL), Lausanne, Switzerland

[d] Departamento de Ciencia de los Materiales, Ingeniería Metalúrgica y Química Inorgánica, Facultad de Ciencias, Universidad de Cádiz, Campus Río San Pedro, Puerto Real (Cádiz) E-11510, Spain

[e] Dipartimento di Chimica Industriale "Toso Montanari", Alma Mater Studiorum Università di Bologna, Viale Risorgimento 4, Bologna 40126, Italy

[f] Center for Chemical Catalysis-C3, Alma Mater Studiorum Università di Bologna, Viale Risorgimento 4, Bologna 40136, Italy

[g] Cardiff Catalysis Institute, School of Chemistry, Cardiff University, Main Building, Park Place, CF10 3AT, Cardiff, United Kingdom

*Corresponding author:

E-mail addresses: alberto.villa@unimi.it, roldanmartineza@cardiff.ac.uk

KEYWORDS

Hydrogen, Hydrous Hydrazine, Catalytic Interface, Ir catalysts, Operando ATR-IR

ABSTRACT

Understanding the structure of a functional catalyst is crucial to disclose the complexity of heterogeneous processes and improve their efficiency. Herein, co-precipitated cobalt-ceria ($CoCeO_x$) oxides doped with Ir ($IrCoCeO_x$) were synthesized and used to assess the performances of metal/oxide interfaces in the $N_2H_4 \cdot H_2O$ decomposition performed in aqueous NaOH. Kinetic experiments in batch showed that CoO is the active phase of $CoCeO_x$ and that the co-presence of Ir and Co ($IrCoCeO_x$) enhanced the H_2 productivity. A comprehensive characterization (X-ray diffraction - XRD, Transmission Electron Microscopy – TEM, X-ray Photoelectron Spectroscopy - XPS, X-ray Absorption Spectroscopy-XAS and *in-situ* Diffuse Reflectance Infrared Fourier Transform Spectroscopy - DRIFTS) combined with robust computational modelling based on the Density Functional Theory (DFT) was employed to attribute the $IrCoCeO_x$ performance enhancement to the Ir/CoO metal/oxide interface, active site of the reaction. On these sites, the improved H_2 productivity in presence of aqueous NaOH was studied *operando* through Modulated Excitation-ATR-IR (ME-ATR-IR) coupled with Phase Sensitive Detection (PSD). The formation

of surface Co-hydroxyl and -imido groups at the Ir/CoO interface induced the preferential breakage of the N-H bond of $N_2H_4 \cdot H_2O$, favouring the production of H_2.

INTRODUCTION

Hydrogen is recognized as a promising energy vector for the future, but its safe and effective storage must be addressed to support the growth of a green economy.[1] Liquid Hydrogen Carriers (LHCs) are chemical compounds easily storable and transportable which can release a high hydrogen content at mild conditions.[2] Many LHCs exist, but the search for CO-free H_2 led to focus in particular on nitrogen-hydrides.[3] Hydrous hydrazine ($N_2H_4 \cdot H_2O$) possesses an H content as high as 8 wt.%, and its decomposition produces either molecular hydrogen and nitrogen or ammonia and nitrogen, the latter being the thermodynamically favoured process.[4]

$N_2H_4 \cdot H_2O$ is a Brønsted base capable of accepting a proton from water according to Equation 1 ($Kc = 1.7 \cdot 10^{-6}$).[5] So, the use of alkali promoters (NaOH and KOH) is an established procedure to enhance the H_2 production, inhibiting the right-hand side of the equilibrium and enhancing the reaction rate.[6] Nonetheless, the role of NaOH on the surface of catalysts remains ambiguous.

$$N_2H_4 + H_2O \leftrightarrow NH_2NH_3^+ + OH^- \quad (1)$$

Great efforts have been made to develop catalysts that selectively decompose $N_2H_4 \cdot H_2O$ to H_2 and N_2 with high catalytic activity, *i.e.*, high H_2 productivity. First-row transition metals (Ni, Co, Fe) present high selectivity at the cost of lower catalytic activity,[7] while noble metals, such as Ir, Ru and Pt, possess high catalytic activity but rather low selectivity. It is widely reported that the coexistence of different metal species leads to intermetallic charge transfer and orbital hybridizations, that synergistically affects the efficiency of bimetallic catalysts compared to the mono-metallic counterparts.[8] Thus, in recent years, bifunctional systems composed of both types

of elements have attracted interest, achieving high catalytic activity and enhanced selectivity,[9] opening up the possibility of applications where high H_2 productivity is crucial, *e.g.*, on-board use.[10] For example, the beneficial effect of a bimetallic Ir-Co interaction has been elucidated for the $N_2H_4{\cdot}H_2O$ decomposition on Al_2O_3 supported catalysts, achieving complete hydrogen generation at ambient conditions.[11]

An alternative procedure to alter the electronic structure of a catalyst is the induction of metal support interactions through metal-oxide interfaces,[12] and the reactive interfaces between transition metal particles and oxide-support were found effective for various catalytic processes.[13] In particular, the interaction between metallic Ir and Co oxides enhanced many chemical transformations, including water oxidation,[14] CO hydrogenation and syngas processing.[15,16]

To this end, in this work Iridium-Cobalt-Cerium ($IrCoCeO_x$) composite was synthesized and compared to $CoCeO_x$, CeO_2 and $IrCeO_2$ to probe the performance of the metal-oxide interfaces in the batch $N_2H_4{\cdot}H_2O$ decomposition. A comprehensive characterization (XRD, XPS, XAS, DRIFT, HR-TEM) of the catalysts elucidated the structure of the composites and a promoting Ir-Co interaction in $IrCoCeO_x$ arising from the synergic Ir/CoO interface. A combination of different computational approaches at the DFT level, including stochastic search to map energy and morphology of supported clusters, was employed to obtain representative models for the catalysts, in agreement with the characterization performed. The systematic adsorption of a model reactant confirmed the performance boost of $IrCoCeO_x$ and assigned the Ir/CoO interface as active site. The role of NaOH was investigated for $IrCoCeO_x$ and a H_2 productivity observed compared to the reaction performed in pure H_2O. Studies on the interaction of hydrazine on a catalyst surface are limited[17–20] and the current literature lacks of mechanistic insights on the NaOH role. Thus, *Operando* attenuated total reflectance infrared (ATR-IR) enhanced with phase sensitive detection

analysis (PSD) was employed to investigate the nature of adsorbates at the solid-liquid interfaces of $IrCoCeO_x$.[21,22] The formation of Co-hydroxyl and -imido species was directly correlated to the enhanced H_2 productivity through preferential breakage of the N-H bond of $N_2H_4{\cdot}H_2O$ due to NaOH.

METHODS

MATERIALS

Hydrous hydrazine ($N_2H_4{\cdot}H_2O$, 98 %), sodium hydroxide (NaOH, ≥98 %), cobalt (II) nitrate hexahydrate ($Co(NO_3)_2{\cdot}6H_2O$, 98 %), cerium (III) nitrate hexahydrate ($Ce(NO_3)_3{\cdot}6H_2O$, 98 %), sodium carbonate (Na_2CO_3, ≥98 %) and iridium (III) chloride ($IrCl_3$, 99.999 %) were acquired from Sigma-Aldrich.

CATALYST SYNTHESIS

$CoCeO_x$ composite oxides were prepared by a rate-controlled co-precipitation method with a 1 M Na_2CO_3 solution, as previously reported.[23] In a typical preparation, the nitrate precursors, $Co(NO_3)_2{\cdot}6H_2O$ and $Ce(NO_3)_3{\cdot}6H_2O$, to achieve a Co/(Co+Ce) loading of 30 wt.%, were added in the desired volume of milliQ water (50 mL/g catalyst). The Co loading was chosen based on previous works, reported to maximize the contact between the two phases, *i.e.*, synergy between the Ce and Co redox couples.[23] The solution was aged for 30 min under 800 rpm stirring. Na_2CO_3 was added at 2 mL/min with a peristaltic pump until a pH of 8.5, monitored with an online pH electrode. The resulting precipitate was aged at room temperature for 3 h, then washed three times with hot distilled water. The obtained precipitate was dried at 373 K overnight and calcined in

static air at 923 K (2 K/min) for 5 h. The desired amount of Ir ($IrCl_3$) was deposited by incipient wetness impregnation to achieve a metal loading of 1 wt%. Finally, both the bare and Ir-doped supports were thermally treated in a vertical tubular furnace in N_2 at 673 K for 2 h and in 10 % H_2 at 473 K for 2 h (both 5 K/min). As reference, pure CoO was prepared through de-hydration Cobalt hydroxide in vacuum at high-temperature, according to the procedure reported elsewhere.[24]

CATALYTIC ACTIVITY

$N_2H_4 \cdot H_2O$ decomposition was performed at a constant reaction temperature of 343 K, under kinetic conditions,[25] using a 27 mL two-necked round bottom flask. Gaseous products evolution was monitored through the *Man On the Moon X104* kit measuring the partial pressures of the released product.[25] Typically, the catalyst ($N_2H_4 \cdot H_2O$ / Ir molar ratio 1000/1) was added to the reactor with 5.0 mL of a 0.5 M NaOH ($N_2H_4 \cdot H_2O$ / NaOH molar ratio 5/1) aqueous solution and heated at the desired temperature. Finally, 150 μL of a 3.3 M hydrous hydrazine aqueous solution was injected to the final mixture with a stirring rate of 1400 rpm. The kinetic profiles were sampled at 4 Hz until the reaction reached equilibrium, indicated by a pressure plateau. To ensure experimental reproducibility and assess measurement uncertainty, all the catalytic tests were performed three times. Selectivity towards H_2 generation (x) was evaluated based on Equation 2. Based on the reaction stoichiometry, at complete conversion, a 100 % H_2 selectivity corresponds to a molar ratio $n(H_2+N_2)/n(N_2H_4)$ of 3, while a value of 0.33 corresponds to 0 %.

$$3N_2H_4 \rightarrow 4(1-x)NH_3 + 6xH_2 + (1+2x)N_2 \quad (2)$$

The absence of gaseous ammonia was verified through MS analysis of the produced gases. Therefore, the selectivity to H_2 was calculated using Equation 3:

$$x=\frac{3\lambda-1}{8},\ \left[\lambda=\frac{n(H_2+N_2)}{n(N_2H_4)}\ \left(\frac{1}{3}\leq\lambda\leq3\right)\right] \quad (3)$$

The conversion of $N_2H_4 \cdot H_2O$ was quantified through a V-730 spectrophotometer (Jasco), using a 1 cm quartz cell, based on the reaction of the remaining substrate, diluted in the 10 mM range and quantitively reacted with an excess of with 4-dimethylaminobenzaldehyde (4-DMAB) additioned with a drod of 37% m/m hydrochloric acid (HCl), resulting in a p-quinone structure that strongly absorbs radiation at 456 nm.[26]

CATALYST CHARACTERIZATION

XRD patterns were collected on a D8ADVANCE diffractometer (Bruker) using Cu $K\alpha_1$ radiation (λ=1.5406 Å). Data were recorded from 20° to 70° 2θ at a step size of 0.02°/s.

TEM experiments were performed on a double Cs aberration-corrected FEI Titan3 Themis 60–300 microscope equipped with a monochromator, a X-FEG gun and a high efficiency XEDS ChemiSTEM, which consists of a 4-windowless SDD detectors. HR-STEM imaging was performed at 200 kV and using a high-angle annular dark-field (HAADF) detector with a camera length of 11.5 cm. The STEM-HAADF technique is sensitive to the atomic number of the elements, whose intensity is roughly proportional to the square of the atomic number (Z^2), and it makes possible to distinguish small nanoparticles supported on light supports (in this work Ir on ceria support). XEDS mappings were performed using a beam current of 200 pA and a dwell time per pixel of 128 μs. To improve the visual quality of the elemental maps obtained, these were filtered using a Gaussian blur of 0.8 using Velox software. Based on the STEM-HAADF images of the catalysts, the diameters of the metal particles randomly selected were measured and the corresponding metal particle size distributions were determined. Based on these particle size

distribution, the average particle diameter (d) was calculated according to the following expression: $d = n_i d_i / n_i$.

X-ray photoelectron spectroscopy (XPS) measurements were performed with a Thermo Scientific K-alpha+ spectrometer. The samples were analysed using a monochromatic Al X-ray source operating at 72 W, with the signal averaged over an oval-shaped area of 600×400 μ. Data were recorded at 150 eV for survey scans and 40 eV for high-resolution (HR) scans with a 1 eV and 0.1 eV step size, respectively. CASAXPS (v2.3.17 PR1.1) was used to analyse the XPS raw data.

CO adsorption experiments were performed *in-situ* in diffuse reflectance mode (DRIFTS) using a Vertex v70 (Bruker) spectrometer equipped with a liquid-nitrogen-cooled mercury cadmium telluride (MCT) detector and a Praying Mantis mirror unit (Harrick). Ca. 100 mg of catalyst sample was loaded into a custom-made cell[27] equipped with a CaF_2 window and a K-type thermocouple. The sample was heated to 473 K in a Ar flow (50 mL/min) and subsequently cooled to 373 K before introducing 1% CO in Ar (50 mL/min) for 30 min. The sample was cleaned in Ar atmosphere for 30 min before the collection and reference spectrum was acquired. All the spectra were acquired using a resolution of 2 cm^{-1} and a scanner velocity of 40 kHz.

Operando attenuated total reflection infrared (ATR-IR) spectroscopy experiments were performed using a Vertex v70 (Bruker) spectrometer equipped with a liquid-nitrogen-cooled MCT detector and a commercial mirror unit. An electrically heated homemade cell was used to monitor the reaction on the catalyst surface. The parallelogram ZnSe prism (45°, 34 mm×20 mm×2 mm; Crystran Ltd.) was coated with a powder film obtained from the evaporation of a aqueous slurry of the catalyst (5 mg/mL H_2O). Solutions and neat solvent were provided from independent glass bottles at a flow rate of 0.3 mL min^{-1} using a peristaltic pump (Reglo 100, Ismatec). At the cell

inlet a 4-ports valve (Cheminert, VICI) enabled fast switching between two different solutions. The switch system was synchronized to the IR spectra acquisition using the OPUS software (Bruker). The cell outlet was collected in a glass bottle connected to a mass spectrometer (MS, Omnistar, Pfeiffer) for the assessment of gaseous products evolution, the catalytic activity and selectivity. The experiments were carried out in a flow cell to increase the control on the reactive environment, preventing the accumulation of surface species.[28,29] In a typical procedure, the solutions were degassed in bubbling Ar for 30 min. After mounting the cell body on the crystal, the temperature was adjusted to the desired value while the catalyst film was equilibrated in H_2O for 30 min. After the water equilibration at 343 K, a reference spectrum was collected. The experiments were performed with diluted aqueous solutions of NaOH (5 mM) and $N_2H_4 \cdot H_2O$ (1 mM). The low concentrations were optimised to enhance the detection of surface species under ME ATR-IR conditions. After the equilibration period and background collection, a typical ME experiment cycle consisted of admitting the first solution into the cell for 125 s, followed by the switch to the second solution for the same amount of time, thus leading to a modulation period of 250 s. Spectra were collected by averaging 10 scans at a scanner velocity of 80 kHz and a spectral resolution of 4 cm^{-1} resulting in a time resolution of 1.25 s/spectrum. A standard experiment consisted of 10 periods. Only the periods at quasi-stationary regime were averaged to improve the S/N ratio, and signal enhancement was achieved by phase sensitive detection (PSD) analysis using a Matlab script. The phase domain spectra were obtained by mathematical treatment of the time-domain data according to Equation 4.

$$A_k\left(\phi_k^{PSD}\right)=\frac{2}{T}\int_0^T A(t)\sin(k\omega t+\phi_k^{PSD})dt \qquad (4)$$

where T is the period length, ω is the stimulation frequency, k is the demodulation index ϕ_k^{PSD} is the demodulation phase angle, and $A(t)$ and $A_k(\phi_k^{PSD})$ are active species respone in time- and phase- domain, respectively.[30]

XAS data were measured at the SuperXAS beamline of the Swiss Light Source (Villigen, Switzerland) facility.[31] The beam originating from the 2.9 T superbend source was collimated using a Si coated mirror at 2.84 mrad (Rh coating for the Ir L3 edge) and subsequently monochromatized with a LN cooled Si 111 QEXAFS monochromator. Data were acquired in transmission mode for the Co-K (7.708 keV) edges with 1.5 bar N_2 filled ion chambers and in fluorescence was employed for the Ir-L_3 edge (11.215 keV) with a PIPS detector.[32] The QEXAFS data were collected for 5 minutes with energy calibration, interpolation, normalisation and averaging using ProQEXAFS.[33] X-ray absorption near edge structure (XANES) processing and extended X-ray absorption fine structure (EXAFS) analysis were performed using the Athena and Artemis software, from the Demeter suite.[34] Data fitting of the EXAFS function of the Ir-L_3 edge for $IrCoCeO_x$ was performed in R space between 1 and 3.5 Å, using Ir-O, Ir-Co and Ir-Ir scattering paths. The amplitude factor of the EXAFS equation (S_0^2) was obtained from the fit of a Ir reference and fixed for all the samples. The energy shift parameter (ΔE_0) was kept constants for all the scattering paths.

COMPUTATIONAL MODELS AND DETAILS

DFT CALCULATIONS

Spin-polarized periodic plane-wave DFT calculations were carried out using the Vienna Ab-initio Simulation Package (VASP).[35] Projected augmented wave pseudo-potentials[36] and revised Perdew-Burke-Ernzerhof (RPBE) functionals were adopted with a kinetic energy of 400 eV

chosen as the cutoff value for the expansion of the plane-waves basis set. RPBE pseudo-potentials were used to obtain accurate adsorption energies. Indeed, for the chemisorption of small molecules on transition metals, including Ir and Co, RPBE results are closer to experiments than PBE.[37,38] In addition, RPBE+U is effective in reproducing the properties of reducible transition metal oxides.[38,39] The strong on-site Coulomb repulsion of Ce 4*f* and Co 3*d* states was accurately reproduced using the Dudarev scheme[40,41] with Hubbard values of 5.0 and 3.3 eV, respectively, and including non-spherical contributions of the gradient of the density in the PAW spheres.[42,43]

Bulk CeO_2 and CoO (Figure S1) were optimized starting from reference data (ICSD-28709 and -9865 respectively for CeO_2 and CoO). The optimization thresholds for electronic energies and ionic forces relaxation were 10^{-5} eV and 0.01 eV/Å, respectively. The Brillouin zone was sampled using a 8 × 8 × 8 **Γ**-centred **k**-point mesh generated through the Monkhorst–Pack method, minimizing any Pulay stress.[44] Ionic positions, lattice parameters, and electronic structure of the bulk systems were analysed to validate the accuracy of the computational setup employed (Figure S1 and Table S1). All surface slabs were generated with the Atomic Simulation Environment (ASE)[45] starting from the optimized bulk systems. Convergence criteria were kept as in the bulk calculations, yet the **k-**points adapted to **Γ**-point. A vacuum of 15 Å was created along the *c*-axis to form the surfaces and avoid any interaction between adjacent images. Cluster-support interfaces were modelled with stochastic procedures; to ease the computational effort, models with two O-Ce-O layers of a *p*(2 × 2) CeO_2 (111) and four Co-O layers of a *p*(4 × 4) CoO (100) were chosen, Figure S1.

The charge density difference (CDD) of supported clusters was calculated using Equation 5, where $\rho(i)$ indicates the electron density of species i.

$$\rho(CDD)=\rho(Combined)-\rho(Surf)-\rho(Cluster) \quad (5)$$

Adsorption energies (E_{ads}) were calculated using Equation 6. Where $E_{reactant}$ is the energy of the isolated reactant, while E_{Cat} and $E_{combined}$ refers to the energy of the catalyst before and after the adsorption of the reactant. Similarly, the adhesion energies (E_{adh}) were calculated using Equation 7, where E_{cat}^{*} is the catalyst fixed in the geometry of adsorption to exclude reconstruction contribution, quantified as the difference of adsorption and adhesion energies for a certain structure (Equation 8).

$$E_{ads}=E_{combined}-E_{cat}-E_{reactant} \quad (6)$$

$$E_{adh}=E_{combined}-E_{cat}^{*}-E_{reactant} \quad (7)$$

$$E_{rec}=E_{ads}-E_{adh} \quad (8)$$

GA-DFT STRUCTURAL OPTIMIZATION

A metal-cluster model simulating the experimentally observed size is prohibitively expensive to compute using electronic structure methods. Despite this, simplified computational models complement experiments with atomic-level insights. Considering the high number of atoms present in the structures, an Ir_8 cluster was employed as a compromise between the representativeness and computational effort of the models.[43] The current choice for Ir_8 is pragmatic, based on selecting a system with a large enough atomic population to resemble the local atomic environment of an Ir nanoparticle, capturing the metal-support interaction realistically but small enough to allow an extensive mapping of energy and morphology of supported clusters.[43] An unbiased Genetic Algorithm based on spin-polarized DFT+U energies (GA-sDFT+U) has been conducted to find the putative global minima of the clusters supported on CeO_2 (111) and CoO (100), in agreement with XRD and HR-TEM results. More than 500 different cluster morphologies and sites were evaluated for each surface. A pool size of 8 members was employed, with crossover

and mutation operations procedures performed employing randomization and displacement operators, respectively. The initial pool members were randomly generated with a cluster-to-surface height of 2.0 Å. A mutation rate of 10% was employed to guarantee the generational variety among the structures.

The energy of all these structures was determined by VASP using a soft optimization protocol, *i.e.*, the thresholds for electronic and ionic relaxation energies, respectively, of 10^{-4} eV and 10^{-3} eV, evaluated at the **Γ**-point and with frozen supports. An increased number of initial non-self-consistent steps and linear mixing involving the metal d-orbitals improved the wavefunction convergence. The Brillouin-zone evaluation was eased using the second-order Methfessel–Paxton method with a smearing width of 0.05 eV. The putative global minima were re-optimized at an electronic and ionic relaxation forces threshold of 10^{-5} eV and 0.02 eV/Å. These optimizations included relaxing the first slab layer to enhance the metal-support interactions and obtain more robust models.

ADSORPTION SCREENING ON SUPPORTED CLUSTERS

Determining adsorption configuration can be challenging on complex and irregular surfaces, and, for example, in the case of supported clusters, it requires the initial determination of all the atoms belonging to the cluster and the adsorption sites. To address these issues, the Delauney tetrahedralization algorithm was employed to classify top, bridge, and hollow adsorption sites of supported clusters through an in-house modified version of the Cluskit package.[46]

On the most stable cluster geometry on CeO_2 (111) and CoO (100), NH_3 was employed as a probe molecule to identify adsorption sites. More than 60 configurations were evaluated after removing the N-N rotational degree of freedom present in N_2H_4. RPBE pseudo-potentials were used to obtain

accurate adsorption energies.[37] All the calculations included the long-range dispersion correction approach by Grimme – DFT-D3 methods with zero-damping,[47,48] an improvement on pure DFT to evaluate molecular interactions.[49,50]

Herein, a soft optimization protocol was employed, *i.e.*, the thresholds for electronic and ionic relaxation energies, respectively, of 10^{-4} eV and 10^{-3} eV at the **Γ**-point only and relaxing all the atoms within a sphere of 4 Å from the probe molecule, including cluster and slab. This radius was selected upon observation of the central distortion during molecular adsorptions. The most stable structures were then re-optimized at higher precision, with electronic and ionic relaxation forces of 10^{-5} eV and 0.02 eV/Å, respectively.

RESULTS AND DISCUSSION

CATALYTIC ACTIVITY

The metal oxides (CeO_2 and $CoCeO_x$) were prepared by co-precipitation and used as support for 1 wt.% Ir ($IrCeO_2$ and $IrCoCeO_x$) catalysts. After activation at high temperature (2h in N_2 at 673 K and 2 h in 10 vol.% H_2 at 473 K), the performance of the catalysts for the $N_2H_4 \cdot H_2O$ decomposition was studied in a batch reactor (343 K), in presence of NaOH (0.5 M, NaOH/ $N_2H_4 \cdot H_2O$ molar ratio 5/1).[51]

The kinetic results are represented in Figure 1a. CeO_2 was completely inactive, and the activity was very shallow even after Ir addition ($IrCeO_2$). Instead, the presence of Co activated the mixed oxide catalysts for the $N_2H_4 \cdot H_2O$ decomposition. $CoCeO_x$ completed the reaction in 40 min with a H_2 selectivity of 35 % and the addition of Ir ($IrCoCeO_x$) clearly boosted the performance, resulting in a 5-fold increase in the catalytic activity and a final H_2 selectivity of 68 %. The reaction temperature was chosen based on a series of experiments performed on $IrCoCeO_x$ (Figure S2). In agreement with previous literature,[52,53] the reaction performed at higher temperature (343 K) resulted in a higher H_2 productivity.

The catalytic data of $CoCeO_x$ pointed to Co as the active phase, thus, to obtain insights into its nature, the performance was compared to that of common Co phases (CoO and Co_3O_4), and of pure CoO_x, prepared by thermal activation of Co_3O_4. $IrCoO_x$ was also prepared but a strong magnetization of the sample was observed after activation, which prevented the execution of the batch catalytic tests due to the presence of the magnetic stirrer. As shown in Figure 1b, $CoCeO_x$, CoO_x and CoO achieved a H_2 selectivity of 35, 27 and 5 %, respectively, and comparable performances in terms of catalytic activity, while Co_3O_4 was completely inactive, suggesting that

CoO is the active phase in $CoCeO_x$ and that its performances are improved compared to pure phase due to the co-precipitation with CeO_2.

The reactions were performed in aqueous NaOH 0.5 M because alkaline solutions are commonly employed to enhance the de-hydrogenation performances of $N_2H_4 \cdot H_2O$ decomposition, Table S2.[5,6,54] The effect of NaOH was demonstrated for $IrCoCeO_x$ through a comparison of the reaction performed in aqueous NaOH and that in pure H_2O (Figure 1c), inducing a two-fold increase of the catalytic activity and of the H_2 selectivity from 15 to 68 %, in agreement with the literature.[6,54]

The importance of the co-presence of Ir and Co in the catalyst and of NaOH in the reaction solution in promoting the reaction has been highlighted. However, durability is crucial for a catalyst to be attractive for commercial applications. Thus, the performances of $IrCoCeO_x$ in presence of NaOH were investigated, by performing 10 consecutive reaction with fresh solutions. Up to about 120 min of reaction time, $IrCoCeO_x$ exhibited a comparable selectivity but a decreased catalytic activity, the H_2 selectivity decreasing from 68 % in 4 min to 63 % in 20 min, Figure 1d and S3. A comparison of the performance of $IrCoCeO_x$ with the recent literature is proposed in Table S2.

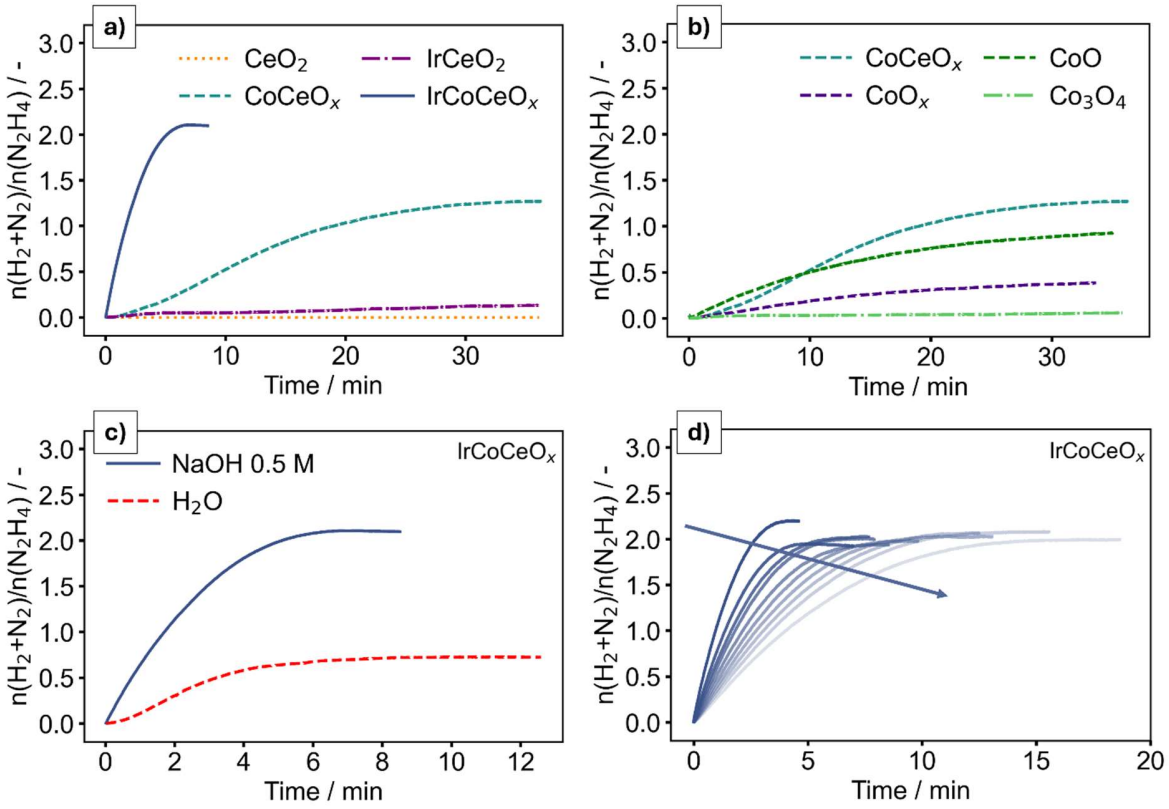

Figure 1. Kinetic profiles for the batch $N_2H_4 \cdot H_2O$ decomposition reaction. a) Comparison between catalysts (NaOH 0.5 M) : CeO_2, $CoCeO_x$, $IrCeO_2$ and $IrCoCeO_x$. b) Activity of the different Co phases. c) Effect of NaOH on $IrCoCeO_x$. d) Stability test for $IrCoCeO_x$ (10 repeated reaction runs), an arrow in is added to guide the eye along the tests. All the experiments were performed at 343 K and 1400 rpm, with 300 µL of a 3.3 M hydrous hydrazine solution in 5 mL of the reported solvent and an $N_2H_4 \cdot H_2O$: Ir molar ratio of 1000:1.

CHARACTERIZATION OF THE METAL/OXIDE INTERFACES

The formation of metal-oxide interfaces often contributes to enhanced performance of catalytic processes.[13,55] To this end, a thorough characterization was employed to elucidate the complexity of the nanocomposites and to allow the correlation of the structural/geometric properties to the kinetic data. The XRD pattern of the metal oxides (Figure 2a) exhibited peaks at 2θ values of 28.3, 32.8, 47.0, 55.7 and 58.4 °, that are characteristics (111), (110), (211), (221), and (220) planes of the of the cubic fluorite CeO_2 structure (Fm$\underline{3}$m).[56] On the other hand, reflections at 2θ of 36.2, 42.2, and 61.1 ° revealed the presence of CoO in $CoCeO_x$.[56] These findings are in well agreement with the active phase suggested by the comparison of $CoCeO_x$ with the common Co phases shown in Figure 1b. As a confirmation, STEM-HAADF images of the $CoCeO_x$ support demonstrated the presence of large independent CeO_2 and CoO domains (Figures 2a, S4). Thus, based on the differences observed in the kinetic experiments (Figure 1a-b), it can be concluded that CoO is the active phase of $CoCeO_x$.

To rationalize the different performances of $IrCeO_2$ and $IrCoCeO_x$, the attention turned to the study of metal-support interactions. The addition of Ir did not modify the structure of the materials and both $IrCeO_2$ and $IrCoCeO_x$ preserved the crystalline phases of the starting materials (Figure S5). In $IrCeO_2$, Ir had an average particle size of 0.68 nm and preferentially interacted with holes and grain boundaries of the support (Figure S6). Differently, in $IrCoCeO_x$ (Figure S7), Ir was well-dispersed over the whole mixed oxide, with an average particle size of 1.26 nm.

The combination of XRD and TEM data revealed that no significant modification of the bulk occurred after Ir deposition, so the surface composition and atomicity of the catalysts were analysed with XPS. The presence of an Ir-Co interaction was indicated by a greater decrease in

the Co *2p* signal (6.4 to 2.4 at.%) with respect to the Ce *3d* (6.7 to 4.3 at.%) observed in the survey scans of $CoCeO_x$ and $IrCoCeO_x$ (Table S3). Confirming this, the oxidation of Co in presence of Ir was observed from the positive shift of the Co 2*p* signal of $IrCoCeO_x$ compared to $CoCeO_x$ (780.4 vs. 779.5 eV, Figure 2c). In agreement, an electron donation to Ir occurred in presence of Co, as observed from the negative shift of the Ir 4*f* signal of $IrCoCeO_x$ compared to $IrCeO_2$, 61.1 and 62.2 eV (Figure S8). The absence of significant changes in the Ce 3*d* region allowed to exclude major modifications in the electronic structure of surface Ce due to Ir or CoO (Figure S8).

The Ir/CoO interaction in $IrCoCeO_x$ was investigated with a combination of *in-situ* CO-DRIFT (Figure 2d) and XAFS (Figure 2e-f). The CO adsorption on $IrCeO_2$ revealed a band in the 2110-2050 cm^{-1} range, attributed to linearly adsorbed CO on Ir species depleted from electron density by the interaction with CeO_2.[57,58] The presence of Co induced a red shift (2085 to 2070 cm^{-1}) of the Ir-C=O signal, closer to the value for metal Ir,[59] and a lower intensity of the white-line at the Ir-L_3 XANES edge for $IrCoCeO_x$, *i.e.*, higher occupation of d-states. The combined information from XPS, CO-DRIFT and XANES suggested a modification of the Ir electronic structure due to electron transfer from Co, which was ultimately attributed to Ir-Co bonds (2.58 ± 0.01 Å) from the FT-EXAFS of $IrCoCeO_x$ (Figure 2f, Figure S9, and Table S4).

Overall, the differences observed in the electronic structure of the metal/oxide interfaces agreed with the results of the kinetic experiments. For $IrCeO_2$ the interaction of small Ir nanoparticles with CeO_2 resulted in electron depletion from Ir and correlated with the shallow activity observed. In $IrCoCeO_x$, the CoO phase anchored to the CeO_2 matrix induced a substantial charge transfer to the Ir nanoparticles through Ir-Co bonds that resulted in the H_2 productivity enhancement observed.

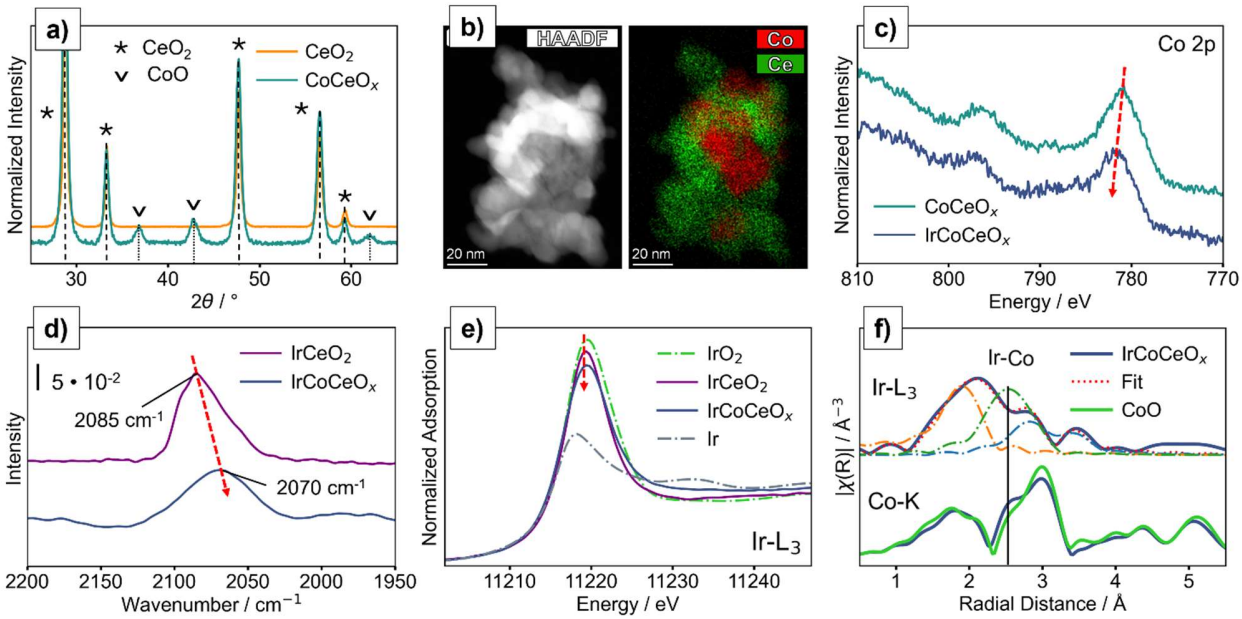

Figure 2. Structural understanding of the catalysts. a) XRD patterns; b) STEM-HAADF image of $CoCeO_x$ with corresponding XEDS mapping for Co and Ce; c) Co 2p HR-XPS spectra; d) DRIFTS spectra of adsorbed CO over $IrCeO_2$ and $IrCoCeO_x$ catalysts at 373 K; e) Ir-L_3 XANES; f) k^2-weighted Ir-L_3 and Co-K edge phase shift corrected FT-EXAFS of $IrCoCeO_x$.

DFT MODELING OF THE METAL/OXIDE INTERFACE

Computational modeling was performed to obtain atomistic scale insights into the Ir interaction with the metal oxides. First, representative models of the materials were constructed based on the thorough characterizations performed. The TEM results confirmed that large and independent CoO domains are clearly distinguished for $CoCeO_x$ and $IrCoCeO_x$ (Figure 2b and S3-4), and their electronic structure assigned the performance enhancement to the charge transfer between Ir and CoO anchored to the CeO_2 matrix. Therefore, based on the XRD prominent peaks, $IrCeO_2$ and $IrCoCeO_x$ were modeled with an Ir cluster supported on CeO_2 (111) and CoO (100) slabs. The

corresponding structural models, before the deposition of the Ir_8 cluster, were employed as a representative of CeO_2 and $CoCeO_x$, respectively.

The putative global minimum configuration of an Ir_8 particle on each slab was identified using the GA-sDFT+U approach, using the cluster energy as the fitness function, *i.e.*, frozen support geometry. The minima were in well agreement with the characterization performed (Figure S10), and the first support layer was relaxed to enhance the metal-support interaction. In Ir_8/CeO_2 (111), Figure S11, Ir was observed to interact with the superficial oxygen of CeO_2 (111), the cluster adsorption energy found (E_{ads} -1.6 eV per Ir atom) is in agreement with previous reports.[60] In Ir_8/CoO (100), Ir induced a reconstruction of the CoO (Figure 3a), resulting in a higly stable interface (E_{ads} -2.7 eV per Ir atom). The presence of Ir-Co bonds led to electron donation towards Ir and localization of positive charge at the cluster-support contact region (Figure 3b).

The charge transfer on the most stable Ir_8 clusters agreed with the electronic structure characterization obtained from XPS, CO-DRIFT, and XAFS (Figure 2c, d, e, and f) and the computational models of Ir_8/CeO_2 (111) and Ir_8/CoO (100) interfaces are found to resemble the key physical properties of $IrCeO_2$ and $IrCoCeO_x$, respectively. Indeed, in $IrCeO_2$, Ir is in a higher oxidation state compared to $IrCoCeO_x$, where Ir-Co bonds modified the electronic structure of Ir and interfacial Co atoms.

To correlate the different metal-support interactions with the kinetic information, NH_3 was employed as simplified probe to screen systematically adsorption configurations on the slabs, supported clusters, and at the cluster-support interfaces of all models (Table 1). Supported clusters are complex and irregular surfaces, and a systematic evaluation of different (more than 30 for each supported system, including cluster, support and interface configurations, see methods for further

details) required to remove the degrees of freedom related to the H_2N-NH_2 bond. Indeed, previous studies demonstrated that the chemisorption of hydrazine on metals involves (H_2N)-H_2N-M bonds,[50,61–64] which as a first approximation were treated here as H_3N-M. Furthermore, previously we also successfully used NH_3 as a probe to identify active sites for N_2H_4 on carbon materials.[65,66]

On the bare CeO_2 slab no favourable adsorption was obtained, while on $IrCeO_2$, the most stable configuration was NH_3 on the Ir cluster (E_{ads} = -0.22 eV, Figure S12), following the inactivity of CeO_2 and the shallow activity of $IrCeO_2$ observed from the kinetic experiments. On $CoCeO_x$ the adsorption energy is more favourable (E_{ads} -2.53 eV, Figure S13), and in presence of Ir the most stable adsorption configuration for NH_3 was at the metal/oxide interface (Figure 3c) with an adsorption energy of -5.50 eV. The highly negative value was mainly due to reconstruction of the active site upon NH_3 adsorption (E_{ads} –5.50 eV, E_{rec} -2.82 eV), compared to the bare oxide ($CoCeO_x$, E_{rec} -0.57 eV) and the superior reactivity of $IrCoCeO_x$ is correlated to the presence of the bimetallic interaction stabilizing the reactant.[67]

The structure of the adsorbed probe molecule (Table 1) was then investigated to correlate the structural parameters and the thermodynamic of adsorptions with the kinetic data, see Table S5 for the full characterization of the adsorbate-catalyst interaction. A positive trend in the M-N bond distance of $IrCeO_2$, $CoCeO_x$ and $IrCoCeO_x$ (2.157 > 2.086 > 2.053 Å) was found with respect to the adsorption energies (-0.22 > -2.53 > -5.50 eV), *i.e.*, the more favourable the process, the shorter the bond distance. This agreed with the H_2 productivity trends observed from the kinetic experiments of the three catalyst, highlighting the effect of the CoO component stabilized by the CeO_2 matrix as well as the promoting effect of Ir and indicated the Ir/CoO interface, and particularly surface Co vicinal to the Ir cluster, as the active site. Furthermore, the comparison of $CoCeO_x$ and $IrCoCeO_x$ highlighted a modification in the N-H bonds distribution induced by the Ir

presence. In particular, the N-H bond closer to the Ir cluster elongated to 1.043 Å, whereas all three N-H bonds remained close to the average value of 1.029 Å on $CoCeO_x$. This is a further evidence of the Ir promotion and confirmed by the H_2 productivity enhancement observed.

Table 1 Adsorption energies for the most stable configurations of the probe molecule for each slab model, metal-nitrogen (d(M-N)), average (d(N-H)) nitrogen-hydrogen, and the longest nitrogen-hydrogen (max(N-H)) bond-distances.

Structure	**Catalyst**	**E_{ads} / eV**	**d(M-N) / Å**	**d(N-H) / Å**	**max(N-H) / Å**
NH_3	/	/	/	1.017	1.017
CeO_2 (111)	CeO_2	> 0	/	/	/
Ir_8/CeO_2 (111)	$IrCeO_2$	-0.22	2.157	1.032	1.033
CoO (100)	$CoCeO_x$	-2.53 (E_{rec} = -0.57)	2.086	1.029	1.031
Ir_8/CoO (100)	$IrCoCeO_x$	-5.50 (E_{rec} =-2.82)	2.053	1.032	1.043

Overall, the atomistic simulations unveiled the synergic nature of the $IrCoCeO_x$ interface. The trends in adsorption energy of the probe molecule on the $IrCoCeO_x$, $CoCeO_x$, and $IrCeO_2$ models allowed to correlate their physical properties to the experimental H_2 productivity of the catalysts and recognize the reactive Ir/CoO interface as the active site for the $N_2H_4 \cdot H_2O$ decomposition. The promoting effect of Ir in $IrCoCeO_x$, rationalized the enhanced H_2 productivity in terms of a significant electron transfer from Co to Ir through Ir-Co bonds, with localization of positive charge at the cluster-support interface (Figure 3b).

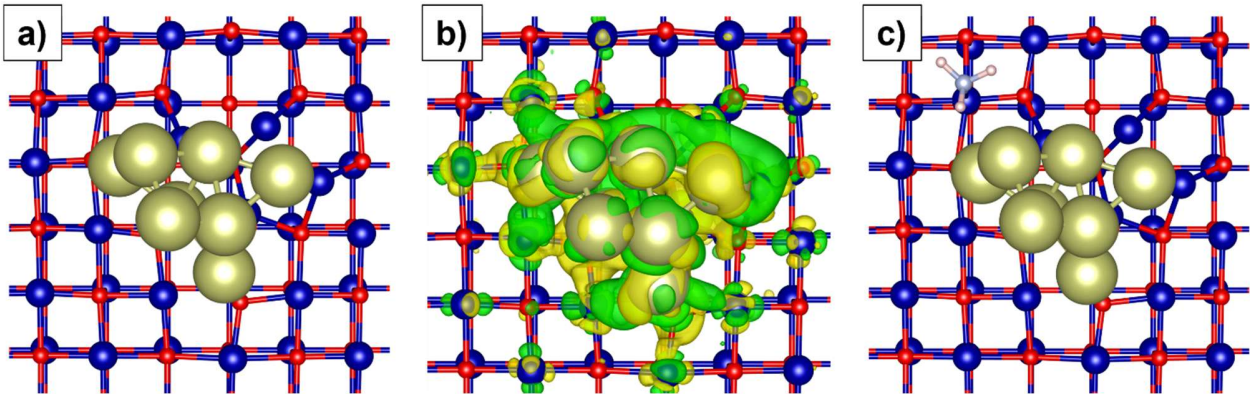

Figure 3. Interaction of Ir with CoO. a) Top view of the most stable Ir_8 cluster on CoO (100); b) corresponding charge density difference (CDD) distribution after cluster adsorption. Yellow and green iso-surfaces denote gain and depletion of electron density respectively, at an iso-surface value is 2×10^{-3} e^- $Å^{-2}$; c) the most stable NH_3 adsorption configuration, demonstrating Ir/CoO metal/oxide interface synergy in $IrCoCeO_x$.

MODULATION EXCITATION ATTENUATED TOTAL REFLECTANCE INFRARED SPECTROSCOPY (ATR-IR) ON THE ROLE OF NAOH

Operando ATR-IR experiments were performed to explain the H_2 productivity enhancement for the reaction performed on $IrCoCeO_x$ in presence of NaOH 0.5 M (Figure 1c) and thus to elucidate the NaOH role on the $N_2H_4{\cdot}H_2O$ decomposition.

Figure 4 shows the phase-resolved spectra obtained from repeated pulses of a $N_2H_4{\cdot}H_2O$ solution in water (Figure 4a) and in aqueous NaOH ($NaOH/N_2H_4{\cdot}H_2O$ = 5; Figure 4b). For the experiment in water, the spectra are dominated by signals at 1394 and 1469 cm^{-1} that are assigned to the $\omega(NH_2)$ modes of $N_2H_4{\cdot}H_2O$, in agreement with the *ex-situ* FT-IR spectra of concentrated $N_2H_4{\cdot}H_2O$ solutions (Figure S14), previous assignments[68,69], and the analysis of PSD data (Figure S15b-c). The presence of NaOH modified the aspect of the region between 1500 and 1250 cm^{-1}. The $\omega(NH_2)$ modes of $N_2H_4{\cdot}H_2O$ (1394 and 1469 cm^{-1}) broadened and additional peaks appeared at 3623, 1430 and 1398 cm^{-1}. The peak at 3623 cm^{-1} was assigned to Co-hydroxyls (Co-OH) species based on control experiments (Figure S16 and S17) and previous reports.[17] The time-resolved data showed an accumulation of these species (Figure S17b), correlating with the deactivation observed in the batch reactor experiments (Figure S3) and the STEM-HAADF image of the used catalyst showing the formation of a layered structure, tentatively attributed to $Co(OH)_2$ (Figure S18). The signals at 1430 and 1398 cm^{-1} were found to possess different kinetics (Figure S17 b-c) and were therefore attributed to independent species.[70] In particular the contribution at 1430 cm^{-1} was assigned to Co-imido (Co-NH) species[17], while the peak at 1398 cm^{-1} was tentatively attributed to the modification of the $\omega(NH_2)$ modes of $N_2H_4{\cdot}H_2O$.

To obtain structure-property relationships, the ATR-IR measurements were correlated to catalytic activity through *operando* steady-state experiments in water and aqueous NaOH with gaseous product detection by mass spectrometry (Figure 4b). The integration of H_2 (m/z =2) and N_2 signals (m/z = 28) was used to estimate H_2 selectivity. Both products evolved intermittently during the experiment, this being due to the formation of bubbles in the tubing leaving the ATR-IR cell because of gas evolution during reaction and the poor solubility in water. We express selectivity through the ratio between the two signals of H_2 and N_2. The reaction performed in water resulted in a low selectivity (H_2/N_2 = 0.31, 15.6% H_2) that correlated with the presence of $\omega(NH_2)$ modes of $N_2H_4{\cdot}H_2O$, suggesting the preferential breakage of the N-N bond of $N_2H_4{\cdot}H_2O$.[4] The presence of aqueous NaOH caused an increase of generated H_2 (H_2/N_2 = 1.21, 60.5% H_2) and the disappearance of the $\omega(NH_2)$ modes of $N_2H_4{\cdot}H_2O$ with the simultaneous formation of Co-OH and Co-NH species. Therefore, it is proposed that NaOH promotes the cooperation of surface Brønsted basic (Co-**O**-Co) and Lewis acid (O-**Co**-O) vicinal sites of the active phase, i.e., CoO enhanced by Ir, favouring the breakage of the N-H bond of $N_2H_4{\cdot}H_2O$ (Figure 5).

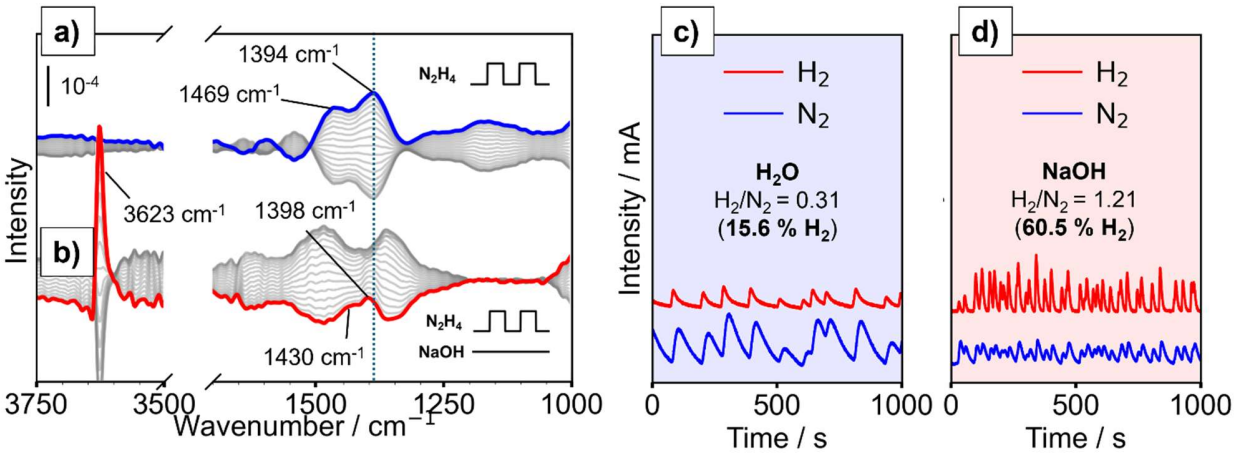

Figure 4 *Operando* ATR-IR spectroscopy on the effect of NaOH on $N_2H_4{\cdot}H_2O$ decomposition on $IrCoCeO_x$. Phase-resolved ATR-IR spectra from modulation experiments of $N_2H_4{\cdot}H_2O$ in water

(a) and in 5/1 mol/mol of NaOH (b). MS signals (m/z =2, H_2; m/z = 28, N_2) from steady-state experiments demonstrating the H_2 productivity enhancement in presence of NaOH (d) compared to H_2O (c).

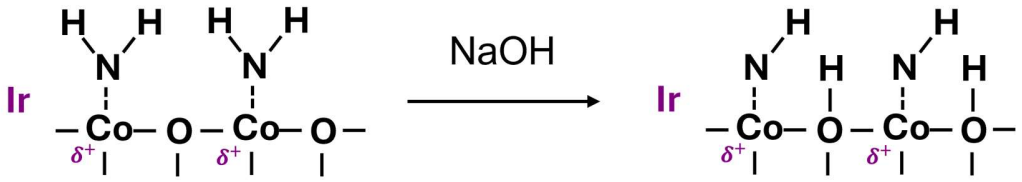

Figure 5 Proposed mechanism for the role of NaOH on the active site of $IrCoCeO_x$.

CONCLUSIONS

Cobalt-Ceria nanocomposites ($CoCeO_x$) impregnated with 1wt. % of Ir ($IrCoCeO_x$) were tested in the $N_2H_4{\cdot}H_2O$ decomposition and compared with CeO_2 and $IrCeO_2$ to probe the performances of the metal/oxide interfaces. The study of $CoCeO_x$ highlighted CoO as the active phase of the catalyst and the presence of Ir ($IrCoCeO_x$) induced a 5-fold increase in the catalytic activity and improved the H_2 selectivity, suggesting a favourable Ir-Co interaction. The effect of aqueous NaOH, an acknowledged promoter of the $N_2H_4{\cdot}H_2O$ decomposition, was then studied for $IrCoCeO_x$ and a two-fold enhancement of the catalytic activity and of the H_2 selectivity from 15 to 68 % observed. A thorough characterization of the catalyst with XRD, TEM, XPS, XAFS, and CO adsorption precisely assigned the performance boost of $IrCoCeO_x$ to the metal/oxide interface of Ir sub-nanometric clusters interacting with CoO. The Ir-Co bonds transferred charge from Co to Ir, resulting in oxidation of surface CoO, which was confirmed to be the active site through DFT calculations using NH_3 as probe molecule. Mechanistic insights on the role of NaOH at the Ir/CoO interface were obtained through *operando* ATR-IR. NaOH operates on the catalyst surface, enhancing the cooperation between vicinal Brønsted basic (Co-**O**-Co) and Lewis acidic (O-**Co**-O) sites of the Ir/CoO interface, inducing a preferential breakage of the N-H bond, *i.e.*, higher H_2 productivity, through Co- hydroxyls and imido groups.

ASSOCIATED CONTENT

Supporting Information.

The Supporting Information is available free of charge.

AUTHOR INFORMATION

Corresponding Author

* alberto.villa@unimi.it

* roldanmartineza@cardiff.ac.uk

Author Contributions

The manuscript was written through contributions of all authors. All authors have given approval to the final version of the manuscript.

Funding Sources

This work has been partially supported by Ministry of Science, Innovation and Universities of Spain with project reference number of PID2020-113809RB-C33. This work has been partially supported from Italian Ministerial grant PRIN 2022 “Green hydrogen from urea-rich wastewater using novel catalytic processes.” – PRIN202223AVILL_01.

Acknowledgment

The authors are grateful to Dr. Adam H. Clark for the XAFS measurements and support during data analysis. The authors acknowledge computing time on the facilities of Supercomputing Wales and the Advanced Research Computing Cardiff (ARCCA) at Cardiff University.

REFERENCES

(1) Edwards, P. P.; Kuznetsov, V. L.; David, W. I. F.; Brandon, N. P. Hydrogen and Fuel Cells: Towards a Sustainable Energy Future. *Energy Policy* **2008**, *36* (12), 4356–4362. https://doi.org/10.1016/j.enpol.2008.09.036.

(2) Modisha, P. M.; Ouma, C. N. M.; Garidzirai, R.; Wasserscheid, P.; Bessarabov, D. The Prospect of Hydrogen Storage Using Liquid Organic Hydrogen Carriers. *Energy & fuels* **2019**, *33* (4), 2778–2796.

(3) Jiang, H.-L.; Singh, S. K.; Yan, J.-M.; Zhang, X.-B.; Xu, Q. Liquid-Phase Chemical Hydrogen Storage: Catalytic Hydrogen Generation under Ambient Conditions. *ChemSusChem* **2010**, *3* (5), 541–549. https://doi.org/https://doi.org/10.1002/cssc.201000023.

(4) Zhang, P.-X.; Wang, Y.-G.; Huang, Y.-Q.; Zhang, T.; Wu, G.-S.; Li, J. Density Functional Theory Investigations on the Catalytic Mechanisms of Hydrazine Decompositions on Ir (1 1 1). *Catal. today* **2011**, *165* (1), 80–88.

(5) Singh, S. K.; Singh, A. K.; Aranishi, K.; Xu, Q. Noble-Metal-Free Bimetallic Nanoparticle-Catalyzed Selective Hydrogen Generation from Hydrous Hydrazine for Chemical Hydrogen Storage. *J. Am. Chem. Soc.* **2011**, *133* (49), 19638–19641. https://doi.org/10.1021/ja208475y.

(6) Wang, H.; Wu, L.; Wang, Y.; Li, X.; Wang, Y. Facile Synthesis of Ni Nanoparticles from

Triangular Ni (HCO3) 2 Nanosheets as Catalysts for Hydrogen Generation from Hydrous Hydrazine. *Catal. Commun.* **2017**, *100*, 33–37.

(7) He, L.; Liang, B.; Li, L.; Yang, X.; Huang, Y.; Wang, A.; Wang, X.; Zhang, T. Cerium-Oxide-Modified Nickel as a Non-Noble Metal Catalyst for Selective Decomposition of Hydrous Hydrazine to Hydrogen. *Acs Catal.* **2015**, *5* (3), 1623–1628.

(8) Singh, A. K.; Xu, Q. Synergistic Catalysis over Bimetallic Alloy Nanoparticles. *ChemCatChem* **2013**, *5* (3), 652–676.

(9) Sanjay, K. S.; Zhang, X. B.; Xu, Q. Room-Temperature Hydrogen Generation from Hydrous Hydrazine for Chemical Hydrogen Storage. *J. Am. Chem. Soc.* **2009**, *131* (29), 9894–9895. https://doi.org/10.1021/ja903869y.

(10) Durbin, D. J.; Malardier-Jugroot, C. Review of Hydrogen Storage Techniques for on Board Vehicle Applications. *Int. J. Hydrogen Energy* **2013**, *38* (34), 14595–14617. https://doi.org/https://doi.org/10.1016/j.ijhydene.2013.07.058.

(11) Firdous, N.; Janjua, N. K.; Qazi, I.; Sarwar Wattoo, M. H. Optimal Co–Ir Bimetallic Catalysts Supported on γ-Al2O3 for Hydrogen Generation from Hydrous Hydrazine. *Int. J. Hydrogen Energy* **2016**, *41* (2), 984–995. https://doi.org/https://doi.org/10.1016/j.ijhydene.2015.10.084.

(12) Schneider, W.; Heyde, M.; Freund, H. Charge Control in Model Catalysis: The Decisive Role of the Oxide–Nanoparticle Interface. *Chem. Eur. J.* **2018**, *24* (10), 2317–2327.

(13) Kim, J.; Choi, H.; Kim, D.; Park, J. Y. Operando Surface Studies on Metal-Oxide Interfaces

of Bimetal and Mixed Catalysts. *ACS Catal.* **2021**, *11* (14), 8645–8677. https://doi.org/10.1021/acscatal.1c02340.

(14) Shan, J.; Ye, C.; Chen, S.; Sun, T.; Jiao, Y.; Liu, L.; Zhu, C.; Song, L.; Han, Y.; Jaroniec, M. Short-Range Ordered Iridium Single Atoms Integrated into Cobalt Oxide Spinel Structure for Highly Efficient Electrocatalytic Water Oxidation. *J. Am. Chem. Soc.* **2021**, *143* (13), 5201–5211.

(15) Cronauer, D. C.; Jacobs, G.; Linganiso, L.; Jeremy Kropf, A.; Elam, J. W.; Christensen, S. T.; Marshall, C. L.; Davis, B. H. CO Hydrogenation: Exploring Iridium as a Promoter for Supported Cobalt Catalysts by TPR-EXAFS/XANES and Reaction Testing. *Catal. Letters* **2011**, *141*, 968–976.

(16) Kang, J.; Fan, Q.-Y.; Zhou, W.; Zhang, Q.; He, S.; Yue, L.; Tang, Y.; Nguyen, L.; Yu, X.; You, Y. Iridium Boosts the Selectivity and Stability of Cobalt Catalysts for Syngas to Liquid Fuels. *Chem* **2022**, *8* (4), 1050–1066.

(17) Amores, J. G.; Escribano, V. S.; Ramis, G.; Busca, G. An FT-IR Study of Ammonia Adsorption and Oxidation over Anatase-Supported Metal Oxides. *Appl. Catal. B Environ.* **1997**, *13* (1), 45–58.

(18) Ramis, G.; Yi, L.; Busca, G. Ammonia Activation over Catalysts for the Selective Catalytic Reduction of NOx and the Selective Catalytic Oxidation of NH3. An FT-IR Study. *Catal. Today* **1996**, *28* (4), 373–380.

(19) Matyshak, V. A.; Krylov, O. V. In Situ IR Spectroscopy of Intermediates in Heterogeneous Oxidative Catalysis. *Catal. today* **1995**, *25* (1), 1–87.

(20) Matyshak, V. A.; Silchenkova, O. N.; Ilichev, A. N.; Bykhovsky, M. Y.; Mnatsakanyan, R. A. Mechanism of the Decomposition of Hydrazine Monohydrate on Pd/Al2O3 Studied by in Situ IR Spectroscopy. *Kinet. Catal.* **2023**, *64* (6), 826–836. https://doi.org/10.1134/S0023158423060101.

(21) Ferri, D.; Bürgi, T.; Baiker, A. In Situ ATR–IR Study of the Adsorption of Cinchonidine on Pd/Al2O3: Differences and Similarities with Adsorption on Pt/Al2O3. *J. Catal.* **2002**, *210* (1), 160–170.

(22) Ferri, D.; Bürgi, T.; Baiker, A. Pt and Pt/Al2O3 Thin Films for Investigation of Catalytic Solid− Liquid Interfaces by ATR-IR Spectroscopy: CO Adsorption, H2-Induced Reconstruction and Surface-Enhanced Absorption. *J. Phys. Chem. B* **2001**, *105* (16), 3187–3195.

(23) Liotta, L. F.; Di Carlo, G.; Pantaleo, G.; Deganello, G. Co3O4/CeO2 and Co3O4/CeO2–ZrO2 Composite Catalysts for Methane Combustion: Correlation between Morphology Reduction Properties and Catalytic Activity. *Catal. Commun.* **2005**, *6* (5), 329–336.

(24) Brauer, G. *Handbook of Preparative Inorganic Chemistry V2*; Elsevier, 2012; Vol. 2.

(25) Bellomi, S.; Barlocco, I.; Chen, X.; Delgado, J. J.; Arrigo, R.; Dimitratos, N.; Roldan, A.; Villa, A. Enhanced Stability of Sub-Nanometric Iridium Decorated Graphitic Carbon Nitride for H 2 Production upon Hydrous Hydrazine Decomposition. *Phys. Chem. Chem. Phys.* **2023**, *25* (2), 1081–1095.

(26) Gojon, C.; Dureault, B. Spectrophotometric Study of the Reaction between Hydrazine and p.Dimethylaminobenzaldehyde. *J. Nucl. Sci. Technol.* **1996**, *33* (9), 731–735.

https://doi.org/10.1080/18811248.1996.9731989.

(27) Nuguid, R. J. G.; Ferri, D.; Kröcher, O. Design of a Reactor Cell for Modulated Excitation Raman and Diffuse Reflectance Studies of Selective Catalytic Reduction Catalysts. *Emiss. Control Sci. Technol.* **2019**, *5* (4), 307–316.

(28) Baranowski, C. J.; Fovanna, T.; Roger, M.; Signorile, M.; McCaig, J.; Bahmanpour, A. M.; Ferri, D.; Krocher, O. Water Inhibition of Oxymethylene Dimethyl Ether Synthesis over Zeolite H-Beta: A Combined Kinetic and in Situ ATR-IR Study. *Acs Catal.* **2020**, *10* (15), 8106–8119.

(29) Campisi, S.; Ferri, D.; Villa, A.; Wang, W.; Wang, D.; Kröcher, O.; Prati, L. Selectivity Control in Palladium-Catalyzed Alcohol Oxidation through Selective Blocking of Active Sites. *J. Phys. Chem. C* **2016**, *120* (26), 14027–14033. https://doi.org/10.1021/acs.jpcc.6b01549.

(30) Baurecht, D.; Fringeli, U. P. Quantitative Modulated Excitation Fourier Transform Infrared Spectroscopy. *Rev. Sci. Instrum.* **2001**, *72* (10), 3782–3792.

(31) Müller, O.; Nachtegaal, M.; Just, J.; Lützenkirchen-Hecht, D.; Frahm, R. Quick-EXAFS Setup at the SuperXAS Beamline for in Situ X-Ray Absorption Spectroscopy with 10 Ms Time Resolution. *J. Synchrotron Radiat.* **2016**, *23* (1), 260–266.

(32) Clark, A. H.; Steiger, P.; Bornmann, B.; Hitz, S.; Frahm, R.; Ferri, D.; Nachtegaal, M. Fluorescence-Detected Quick-Scanning X-Ray Absorption Spectroscopy. *J. Synchrotron Radiat.* **2020**, *27* (3), 681–688.

(33) Clark, A. H.; Imbao, J.; Frahm, R.; Nachtegaal, M. ProQEXAFS: A Highly Optimized Parallelized Rapid Processing Software for QEXAFS Data. *J. Synchrotron Radiat.* **2020**, *27* (2), 551–557.

(34) Ravel, B.; Newville, M. ATHENA, ARTEMIS, HEPHAESTUS: Data Analysis for X-Ray Absorption Spectroscopy Using IFEFFIT. *J. Synchrotron Radiat.* **2005**, *12* (4), 537–541.

(35) Kresse, G. Ab Initio Molecular Dynamics for Liquid Metals. *J. Non. Cryst. Solids* **1995**, *192–193* (1), 222–229. https://doi.org/10.1016/0022-3093(95)00355-X.

(36) Kresse, G.; Joubert, D. From Ultrasoft Pseudopotentials to the Projector Augmented-Wave Method. *Phys. Rev. B* **1999**, *59* (3), 1758–1775. https://doi.org/10.1103/PhysRevB.59.1758.

(37) Hammer, B.; Hansen, L. B.; Nørskov, J. K. Improved Adsorption Energetics within Density-Functional Theory Using Revised Perdew-Burke-Ernzerhof Functionals. *Phys. Rev. B* **1999**, *59* (11), 7413–7421. https://doi.org/10.1103/PhysRevB.59.7413.

(38) Hafner, J. Ab-initio Simulations of Materials Using VASP: Density-functional Theory and Beyond. *J. Comput. Chem.* **2008**, *29* (13), 2044–2078.

(39) Getsoian, A. "Bean"; Bell, A. T. The Influence of Functionals on Density Functional Theory Calculations of the Properties of Reducible Transition Metal Oxide Catalysts. *J. Phys. Chem. C* **2013**, *117* (48), 25562–25578.

(40) Dudarev, S. L.; Botton, G. A.; Savrasov, S. Y.; Humphreys, C. J.; Sutton, A. P. Electron-Energy-Loss Spectra and the Structural Stability of Nickel Oxide: An LSDA+U Study. *Phys. Rev. B* **1998**, *57* (3), 1505–1509. https://doi.org/10.1103/PhysRevB.57.1505.

(41) Anisimov, V. I.; Zaanen, J.; Andersen, O. K. Band Theory and Mott Insulators: Hubbard U Instead of Stoner I. *Phys. Rev. B* **1991**, *44* (3), 943–954. https://doi.org/10.1103/PhysRevB.44.943.

(42) Cadi-Essadek, A.; Roldan, A.; Santos-Carballal, D.; Ngoepe, P. E.; Claeys, M.; de Leeuw, N. H. DFT+ U Study of the Electronic, Magnetic and Mechanical Properties of Co, CoO, and Co3O4. *South African J. Chem.* **2021**, *74* (1), 8–16.

(43) Liu, J.-X.; Su, Y.; Filot, I. A. W.; Hensen, E. J. M. A Linear Scaling Relation for CO Oxidation on CeO2-Supported Pd. *J. Am. Chem. Soc.* **2018**, *140* (13), 4580–4587.

(44) Pack, J. D.; Monkhorst, H. J. "special Points for Brillouin-Zone Integrations"-a Reply. *Phys. Rev. B* **1977**, *16* (4), 1748–1749. https://doi.org/10.1103/PhysRevB.16.1748.

(45) Larsen, A. H.; Mortensen, J. J.; Blomqvist, J.; Castelli, I. E.; Christensen, R.; Dułak, M.; Friis, J.; Groves, M. N.; Hammer, B.; Hargus, C. The Atomic Simulation Environment—a Python Library for Working with Atoms. *J. Phys. Condens. Matter* **2017**, *29* (27), 273002.

(46) SINGROUP. Cluskit https://github.com/SINGROUP/cluskit.

(47) Sure, R.; Antony, J.; Grimme, S. Blind Prediction of Binding Affinities for Charged Supramolecular Host–Guest Systems: Achievements and Shortcomings of DFT-D3. *J. Phys. Chem. B* **2014**, *118* (12), 3431–3440.

(48) Ehrlich, S.; Moellmann, J.; Reckien, W.; Bredow, T.; Grimme, S. System-Dependent Dispersion Coefficients for the DFT-D3 Treatment of Adsorption Processes on Ionic Surfaces. *ChemPhysChem* **2011**, *12* (17), 3414–3420.

(49) Fang, H.; Roldan, A.; Tian, C.; Zheng, Y.; Duan, X.; Chen, K.; Ye, L.; Leoni, S.; Yuan, Y. Structural Tuning and Catalysis of Tungsten Carbides for the Regioselective Cleavage of C–O Bonds. *J. Catal.* **2019**, *369*, 283–295. https://doi.org/10.1016/j.jcat.2018.11.020.

(50) Lu, X.; Francis, S.; Motta, D.; Dimitratos, N.; Roldan, A. Mechanistic Study of Hydrazine Decomposition on Ir(111). *Phys. Chem. Chem. Phys.* **2020**, *22* (7), 3883–3896. https://doi.org/10.1039/c9cp06525c.

(51) Motta, D.; Barlocco, I.; Bellomi, S.; Villa, A.; Dimitratos, N. Hydrous Hydrazine Decomposition for Hydrogen Production Using of Ir/CeO2: Effect of Reaction Parameters on the Activity. *Nanomaterials* **2021**, *11* (5), 1340.

(52) Singh, A. K.; Yadav, M.; Aranishi, K.; Xu, Q. Temperature-Induced Selectivity Enhancement in Hydrogen Generation from Rh–Ni Nanoparticle-Catalyzed Decomposition of Hydrous Hydrazine. *Int. J. Hydrogen Energy* **2012**, *37* (24), 18915–18919.

(53) Adamou, P.; Bellomi, S.; Harkou, E.; Chen, X.; Delgado, J. J.; Dimitratos, N.; Manos, G.; Villa, A.; Constantinou, A. Hydrous Hydrazine Decomposition over Rh/Al2O3 Catalyst: Experimental and CFD Studies. *Chem. Eng. J.* **2024**, 152715.

(54) He, L.; Huang, Y.; Wang, A.; Wang, X.; Chen, X.; Delgado, J. J.; Zhang, T. A Noble-Metal-Free Catalyst Derived from Ni-Al Hydrotalcite for Hydrogen Generation from N2H4· H2O Decomposition. *Angew. Chemie* **2012**, *124* (25), 6295–6298.

(55) Najafishirtari, S.; Guglieri, C.; Marras, S.; Scarpellini, A.; Brescia, R.; Prato, M.; Righi, G.; Franchini, A.; Magri, R.; Manna, L. Metal-Support Interaction in Catalysis: The Influence of the Morphology of a Nano-Oxide Domain on Catalytic Activity. *Appl. Catal. B Environ.*

2018, *237*, 753–762.

(56) Liotta, L. F.; Di Carlo, G.; Pantaleo, G.; Venezia, A. M.; Deganello, G. Co3O4/CeO2 Composite Oxides for Methane Emissions Abatement: Relationship between Co3O4–CeO2 Interaction and Catalytic Activity. *Appl. Catal. B Environ.* **2006**, *66* (3), 217–227. https://doi.org/https://doi.org/10.1016/j.apcatb.2006.03.018.

(57) Aguirre, A.; Zanella, R.; Barrios, C.; Hernández, S.; Bonivardi, A.; Collins, S. E. Gold Stabilized with Iridium on Ceria–Niobia Catalyst: Activity and Stability for CO Oxidation. *Top. Catal.* **2019**, *62*, 977–988.

(58) Alexeev, O.; Gates, B. C. Iridium Clusters Supported on γ-Al2O3: Structural Characterization and Catalysis of Toluene Hydrogenation. *J. Catal.* **1998**, *176* (2), 310–320.

(59) Vázquez-Parga, D.; Jurado, A.; Roldan, A.; Viñes, F. A Computational Map of the Probe CO Molecule Adsorption and Dissociation on Transition Metal Low Miller Indices Surfaces. *Appl. Surf. Sci.* **2023**, *618*, 156581.

(60) Piotrowski, M. J.; Tereshchuk, P.; Da Silva, J. L. F. Theoretical Investigation of Small Transition-Metal Clusters Supported on the CeO2(111) Surface. *J. Phys. Chem. C* **2014**, *118* (37), 21438–21446. https://doi.org/10.1021/jp505216y.

(61) Tafreshi, S. S.; Roldan, A.; De Leeuw, N. H. Hydrazine Network on Cu(111) Surface: A Density Functional Theory Approach. *Surf. Sci.* **2015**, *637–638*, 140–148. https://doi.org/10.1016/j.susc.2015.04.001.

(62) Tafreshi, S. S.; Roldan, A.; De Leeuw, N. H. Micro-Kinetic Simulations of the Catalytic

Decomposition of Hydrazine on the Cu(111) Surface. *Faraday Discuss.* **2017**, *197* (0), 41–57. https://doi.org/10.1039/c6fd00186f.

(63) Genç, A. E.; Küçük, H.; Alp, I. O.; Akça, A. Hydrazine Decomposition on Nickel-Embedded Graphene. *Int. J. Hydrogen Energy* **2020**, *45* (58), 33407–33418.

(64) Deng, Z.; Lu, X.; Wen, Z.; Wei, S.; Liu, Y.; Fu, D.; Zhao, L.; Guo, W. Mechanistic Insight into the Hydrazine Decomposition on Rh (111): Effect of Reaction Intermediate on Catalytic Activity. *Phys. Chem. Chem. Phys.* **2013**, *15* (38), 16172–16182.

(65) Barlocco, I.; Bellomi, S.; Tumiati, S.; Fumagalli, P.; Dimitratos, N.; Roldan, A.; Villa, A. Selective Decomposition of Hydrazine over Metal Free Carbonaceous Materials. *Phys. Chem. Chem. Phys.* **2022**, *24* (5), 3017–3029. https://doi.org/10.1039/d1cp05179b.

(66) Bellomi, S.; Barlocco, I.; Tumiati, S.; Fumagalli, P.; Dimitratos, N.; Roldan, A.; Villa, A. Effects of Oxygen Functionalities on Hydrous Hydrazine Decomposition over Carbonaceous Materials. *Dalt. Trans.* **2023**, *52* (43), 15871–15877.

(67) Barlocco, I.; Capelli, S.; Lu, X.; Bellomi, S.; Huang, X.; Wang, D.; Prati, L.; Dimitratos, N.; Roldan, A.; Villa, A. Disclosing the Role of Gold on Palladium–Gold Alloyed Supported Catalysts in Formic Acid Decomposition. *ChemCatChem* **2021**, *13* (19), 4210–4222.

(68) Paget, D.; Berkovits, V. L.; Ulin, V. P.; Ozanam, F.; Dumas, P.; Kubsky, S.; Lahlil, K.; Bideux, L.; Monier, G. Real Time Infra-Red Absorption Analysis of Nitridation of GaAs (001) by Hydrazine Solutions. *J. Electrochem. Soc.* **2013**, *160* (4), H229.

(69) Durig, J. R.; Bush, S. F.; Mercer, E. E. Vibrational Spectrum of Hydrazine-d 4 and a Raman Study of Hydrogen Bonding in Hydrazine. *J. Chem. Phys.* **1966**, *44* (11), 4238–4247.

(70) Urakawa, A.; Ferri, D.; Nuguid, R. J. G. Modulation Excitation Spectroscopy (MES). In *Springer Handbook of Advanced Catalyst Characterization*; Springer, 2023; pp 967–977.

TOC